Supplement of The Cryosphere, 16, 2617–2628, 2022
https://doi.org/10.5194/tc-16-2617-2022-supplement

The Cryosphere Open Access EGU

Supplement of

Formation of glacier tables caused by differential ice melting: field observation and modelling

Marceau Hénot et al.

Correspondence to: Nicolas Taberlet (nicolas.taberlet@ens-lyon.fr)

FIG. S1. Pictures of rocks 1 to 4 (see table 1 of the main text) at the begining and at the end of the observation.

Air temperature measurement on site and at the automated Requin weather station. The model used in the article relies on meteorological data measured at the Requin automatic weather station (AWS) located on the edge of the glacier approximately 3 km away from the table measurement site (see fig. 2a of the main text) and 800 m higher in altitude. While we do not expect the solar irradiation or the wind velocity to change much between these two locations, the air temperature is likely to be affected by the altitude difference as well as the proximity of the glacier. Between 18/06/2021 and 06/07/2021 we measured the air temperature 3 m above the glacier surface at the table measurement site using a thermocouple and a home-made autonomous recording device. These data are plotted in fig. S2a alongside with the data from the Requin AWS. This shows that the air temperature onsite can be deduced from the Requin AWS data by adding a 2.5°C offset (see fig. S2b and c).

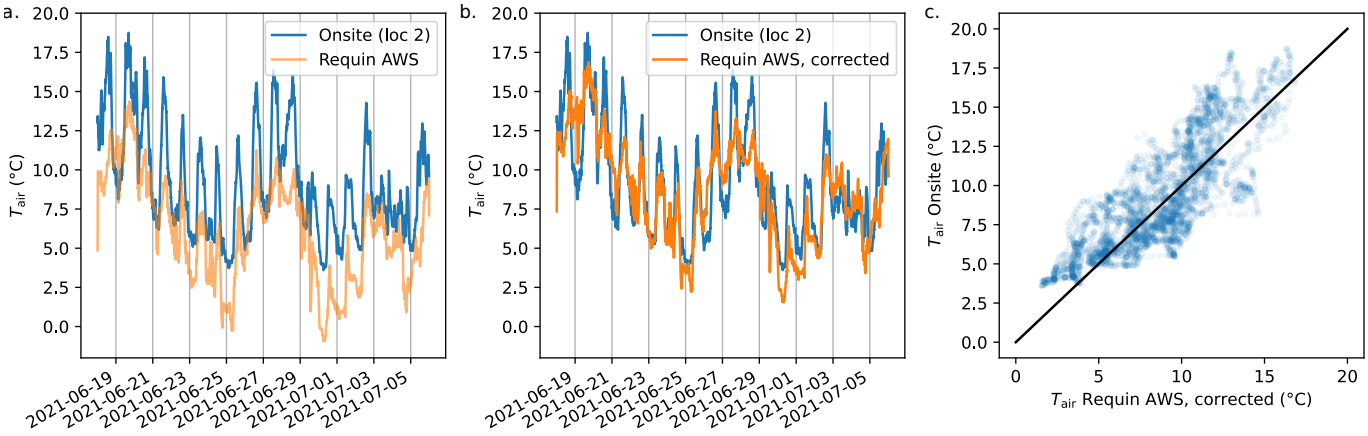

FIG. S2. (a, b) Air temperature T_{air}, 3 m above the ground surface, measured at the Requin AWS (light orange on a) and on the table measurement site (blue) (see location 2 in fig. 2 of the main text). The difference in location and altitude can be taken into account by correcting the AWS data by adding an 3°C offset (orange on b). (c) T_{air} measured on site versus corrected from the AWS data.

Adjustment of ice albedo and surface roughness length. The measured ice ablated thickness $z_{\text{ice}}(t)$ of period A and B was used to adjust the two parameters (α_{ice} and z_0) of the model described in section 3.1 of the main text by minimising the mean squared deviation (MSD). As shown in fig. S3, the best parameter values are $\alpha_{\text{ice}} = 0.30$ and $z_0 = 0.34$ mm.

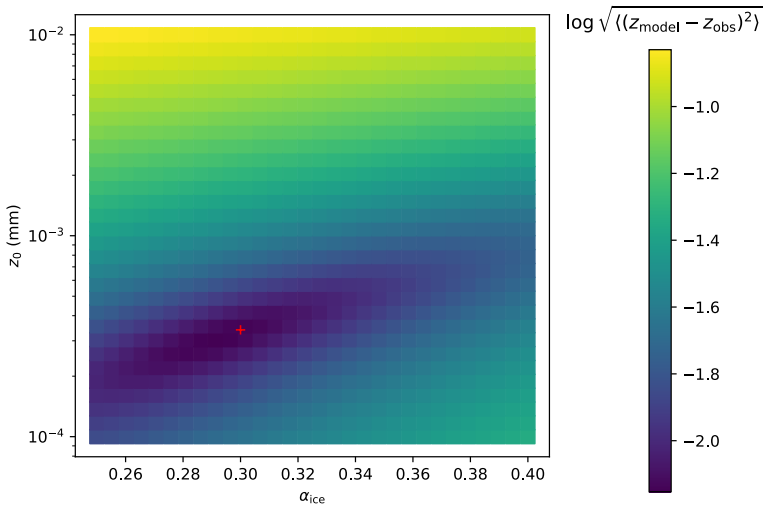

FIG. S3. Sensibility on the MSD of the adjustable parameters z_0 and α_{ice}. The red cross corresponds to the best parameters.

Granite albedo. The spectral reflectivity $R(\lambda)$ of weathered granite was measured by [1] between $\lambda_1 = 400$ nm and $\lambda_2 = 750$ nm. We used this data to compute the granite albedo:

$$\alpha_{\text{granite}} = \frac{\int_{\lambda_1}^{\lambda_2} R(\lambda)\Phi(\lambda)\mathrm{d}\lambda}{\int_{\lambda_1}^{\lambda_2} \Phi(\lambda)\mathrm{d}\lambda} \quad , \quad \Phi(\lambda) \propto \frac{1}{\lambda^5}\frac{1}{e^{hc/(\lambda kT)}-1} \tag{1}$$

where $\Phi(\lambda)$ is the spectral distribution of the solar radiation, estimated from Planck's law. h is the Planck constant, c the speed of light, k the Boltzmann constant and $T = 5780$ K the sun surface temperature. This leads to $\alpha_{\text{granite}} = 0.18$.

Assumption on area of contact between the rock and the ice. In our model, the contact area A_{base} between the rock and the ice is assumed to stay constant equal to its initial value $A^0_{\text{base}} = d_1 d_2$. This simple hypothesis needs to be discussed as that this area clearly diminishes as the ice foot grows (see for instance fig. 1c of the main text). For rock 1, the area is almost divided by two after 200 h. By letting the contact area be diminished by a factor f ($A_{\text{base}} = fA^0_{\text{base}}$) the model developed in the article yields the same results as long as the aspect ratio of the rock is replaced by an effective aspect ratio $\beta_{\text{eff}} = \beta + f/4$. For rock 1 ($\beta = 0.23$), with $f = 0.5$, this leads to $\beta_{\text{eff}} = 0.36$. Yet, as visible in fig. 6 of the main article, in the table formation regime, the ratio $\langle H/H_{\text{ice}}\rangle$ and thus the ice foot growth dynamics, only show a weak dependence with the aspect ratio (of the order of the error bar) which justify the simple assumption.

Assumption on the rock area illuminated by the sun. In our model, we assume that, on average, the solar irradiation Φ is received by a rock on an area $\langle A_{\text{sun}}\rangle = d_1 d_2$ corresponding to the surface area of the top of the rock. In the following we discuss this assumption. Let us consider a 2D rock (see fig. S4a) of thickness h and width d illuminated by a solar irradiation Φ and let θ be the angle between the sun direction and the vertical direction. The heat flux (per unit of depth) received by the rock from the sun is:

$$q_{\text{sun}\to\text{rock}}(\theta) = \Phi d\,[\cos\theta + \beta\sin\theta] \tag{2}$$

where $\beta = h/d$ is the aspect ratio of the rock. During a day, the angle θ goes to $-\theta_0$ to θ_0. The mean heat flux is:

$$\langle q_{\text{sun}\to\text{rock}}\rangle = \frac{1}{\theta_0}\int_0^{\theta_0} q_{\text{sun}\to\text{rock}}(\theta)\mathrm{d}\theta = \Phi d\,[\sin\theta_0 + \beta(1-\cos\theta_0)] \tag{3}$$

As shown in fig S4b, for $\theta_0 = 75°$ and a rock aspect ratio β lying between 0.1 and 0.8, the result of eq 3 differs from Φd by less than 20 %, which justifies the assumption made in the model.

Effect of the geometrical amplification in the model. The model developed in section 3.2 of the main text rely on a 1D conduction model but takes into account the 3D geometry of the problem in the estimation of $d_{1\text{D}}$ but more importantly by taking into account the fact that longwave and turbulent fluxes are exchanged with the environment on the side of the rocks and not only on the top surface. This leads to an geometrical amplification effect of the cooling (or warming for smaller rocks). Fig S5 illustrates the importance of this aspect of the modelisation

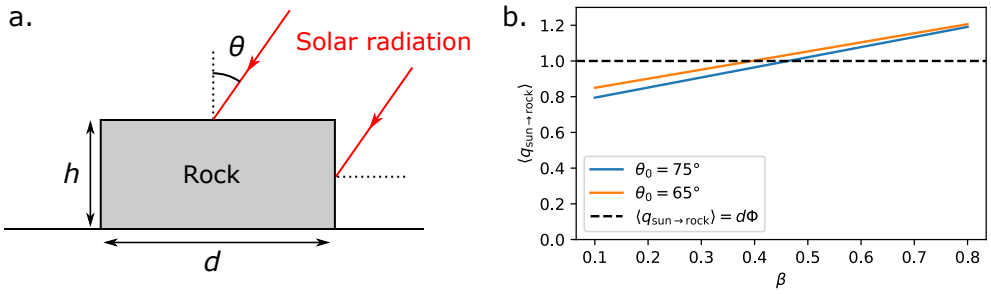

FIG. S4. (a) Schematics of a rock receiving solar irradiation. (b) Mean heat flux received by the rock from the sun given by eq. 3 (solid lines). The dashed line corresponds to the assumption made in the model.

by displaying measurements of $T_{\text{rock}}(t)$ for rock 3 (using a thermocouple attached at the top of the rock) which has a high aspect ratio $\beta = 0.49$ meaning that its side surface is twice as large as its top surface. The rock surface temperature predicted by the model described in the main text (in dark purple) shows a qualitative agreement with the observation (see next paragraph for comments on the differences) and is, on average over the period, less than 1°C lower than the measured temperature. The grey line display $T_{\text{rock}}(t)$ for a purely 1D version of the model (the only difference with the previous version are $d_{\text{1D}} = h$ and all fluxes are exchanged on the same surface A_{base}). This version leads to unrealistic temperature during sunlight (reaching 100 to 200°C) and predicts a surface temperature on average 12°C above what is measured.

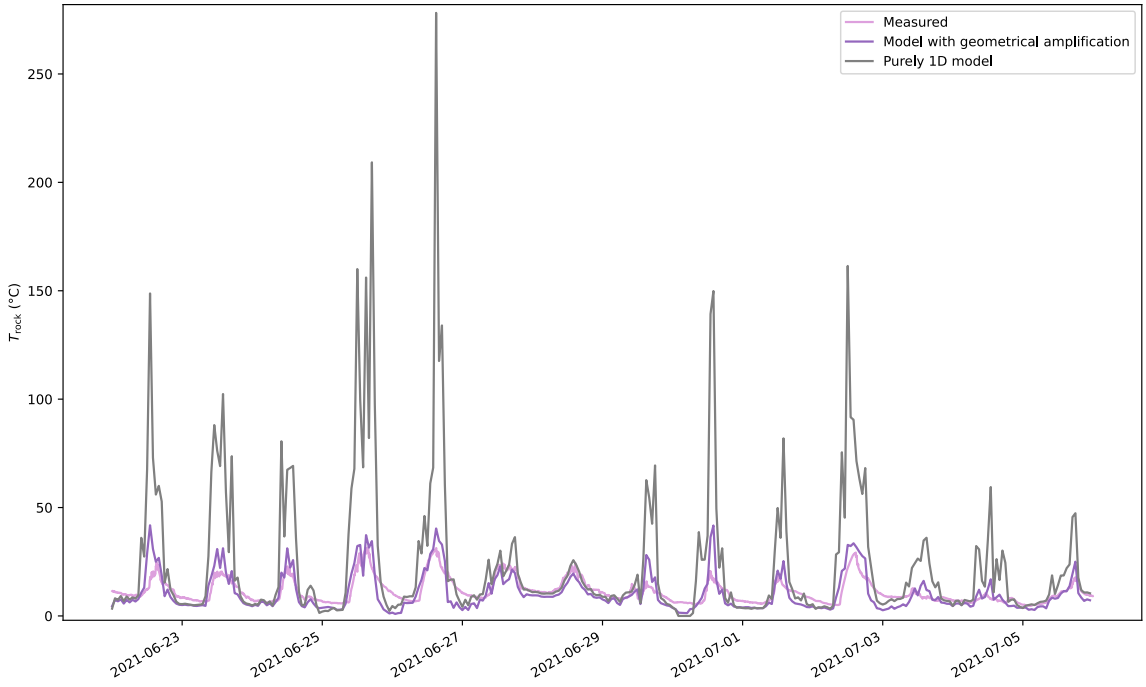

FIG. S5. Surface temperature T_{rock} of rock 3 measured using a thermocouple between the 22 June and the 6 July 2021 (light purple). The dark purple line corresponds to the prediction of the model described in section 3.2 of the main text (taking into account a geometrical amplification effect) while the grey line corresponds to the prediction of a purely 1D model ($d_{\text{1D}} = h$ and all the fluxes are received on the same surface area).

Discussion on the transient heat flux effect. In the model developed in section 3.2 the main text, the transient heat flux effect were neglected under the assumption of a quasi-static process (the heat flux received at the top of the rock is instantaneously transmitted to the ice underneath). Strictly this is not true due to the thermal inertia of the rock. An order of the transient thermal time $t_{\text{transient}}$ can be roughly estimated by balancing the thermal energy stored in the rock between the night and the day and the solar radiative flux received on its top surface:

$$h A_{\text{base}} c_{\text{rock}} \rho_{\text{rock}} \Delta T_{\text{rock}} = t_{\text{transient}} A_{\text{base}} (1 - \alpha_{\text{rock}}) \phi_{\text{max}} \tag{4}$$

where $c_{\mathrm{rock}} \approx 800$ J kg^{-1} K^{-1} is the thermal capacity of of the rock, $\rho_{\mathrm{rock}} \approx 2700$ kg m^{-3} is its density, $\phi_{\max} \approx 1000$ W m^{-2} is the solar flux during sunlight and ΔT_{rock} the typical amplitude of diurnal rock surface temperature variation which if of the order of 20 K for rocks 1 to 4. This leads to respectively $t_{\mathrm{transient\ 3}} \approx 25$ h and $t_{\mathrm{transient\ 4}} \approx 1.4$ h for the thicker and thinner rocks. This has to be compared to the typical time of variation of $\Phi(t)$ which is close to 2 h. The transient effects are thus expected play a role for rock 3 but not for rock 4. It is indeed what can be observed on $T_{\mathrm{rock}}(t)$ in figure S5 and 6 of the main text. No delays are perceptible for rock 4 between the measured and modelled values which is not the case of rock 3 (especially for cooling). The hourly resolved formation dynamic of the structure will therefore not be accurately predicted by our simple model in the case of a metric thick rock such as rock 3. However, the heat fluxes being weakly non-linear with T_{rock} the daily averaged ablation rate under the rock, and thus the global dynamic over the formation period, will be correctly estimated.

Ice ablation during period C: from 27/05 to 03/06/2021. Fig. S6 shows the ablated ice thickness predicted by the model from meteorological data leading to $H_{\mathrm{ice}} = 0.45 \pm 0.05$ m during period C.

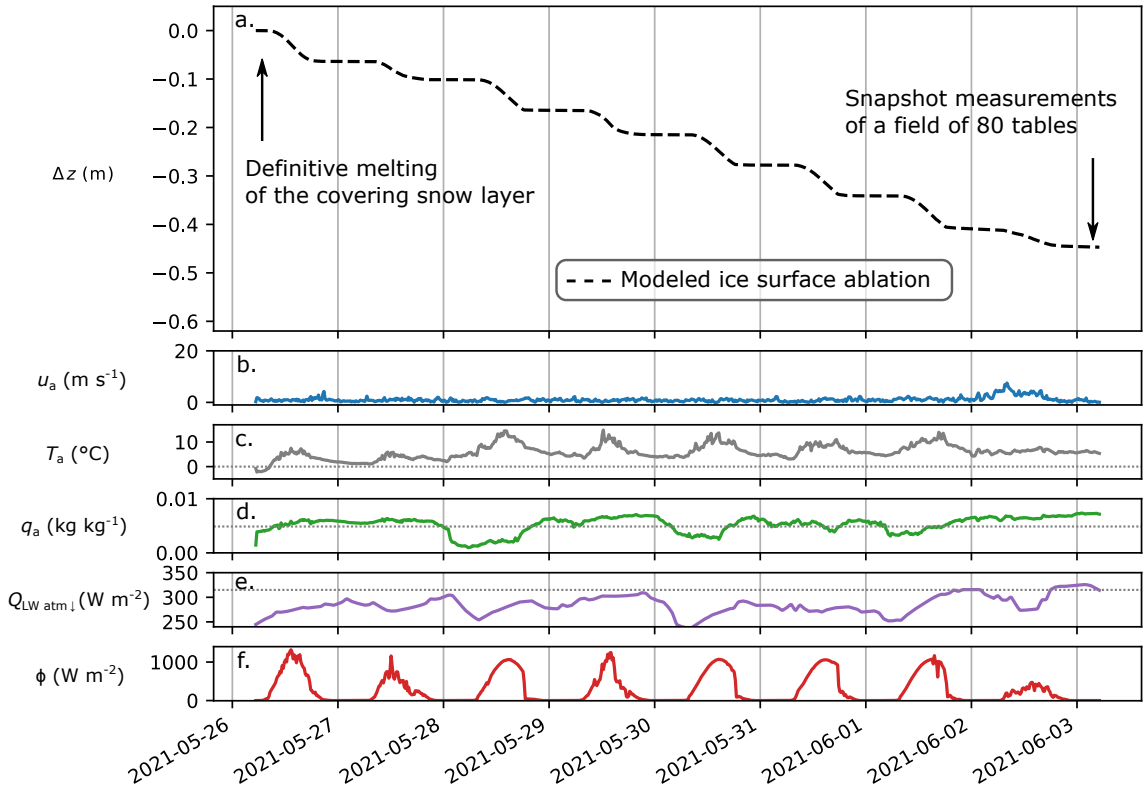

FIG. S6. Ice ablation Δz during period C predicted by the model (see section 3.1 of the main text) using the meteorological data shown (wind speed u_a (b), air temperature T_a (c), specific humidity (d), incoming shortwave radiation $Q_{\mathrm{LW\ atm}\downarrow}$ (e) and solar radiation Φ (f)). The beginning of period C was determined from the observation made using the Montenvers webcam [2] that the covering snow layer (on location 1 in fig. 2a of the main text) definitively melted on 27 May 2021.

[1] R. D. Watson, Spectral reflectance and photometric properties of selected rocks, Remote Sensing of Environment **2**, 95 (1971).
[2] Montenvers webcam, https://www.bergfex.fr/chamonix-mont-blanc/webcams/c3944/ (2021).